

Fast Multigrid Simulations of Pinning in REBCO with Highly Resistive Nanorods

C.W.W. Haddon and D.P. Hampshire

Abstract—A geometric multigrid method is applied to the frozen-field time-dependent Ginzburg–Landau equations for anisotropic superconductors with spatially varying material properties. This reduces the simulation time for critical current determination in large 3D systems by up to two orders of magnitude compared with a single grid. Critical current density calculations are presented for a model of REBCO tape with nanorod artificial pinning centers. The model consists of an anisotropic superconducting matrix with embedded nanorods which are treated as isotropic highly resistive cylinders. The effects of varying the density, splay, and conductivity of the nanorods are considered. Increasing the resistivity of the nanorods profoundly affects the critical current density in high fields, where current paths are percolative in the vicinity of matrix-pin interfaces and persist well above the upper critical field of the superconducting matrix.

I. INTRODUCTION

The critical current densities of high-field superconductors are usually understood in terms of the pinning of fluxons by defects in the superconducting material. In REBCO coated conductors, these defects include natural pinning centers such as dislocations and twin boundaries, and artificial pinning centers (APCs) such as oxide nanoparticles or nanorods. In pulsed laser deposition, for example, nanorod APCs are produced by doping the YBCO target with BaZrO₃ (BZO) impurities [1]. In the deposited film, these impurities agglomerate into nanoparticles which self-assemble into columnar nanorods aligned with the crystal *c*-axis [2], [3]. The nanorods are thought to act as strong pinning centers because of the sharp boundary between the superconducting YBCO and the insulating BZO [4].

Aligned BZO nanorods result in *c*-axis correlated pinning with a peak in J_c as a function of field angle when $B \parallel c$ -axis. It has been demonstrated that some degree of splay, so that the nanorods are not oriented perfectly along the *c*-axis, can broaden the $B \parallel c$ peak and improve the critical current density by producing an entangled vortex matter ground state [5]–[7]. However, it has also been shown that films in which the nanorods are dense and highly aligned across the film thickness demonstrate exceptionally high critical current densities [8], [9].

Manuscript receipt and acceptance dates will be inserted here. This work is funded by EPSRC grant EP/L01663X/1 that supports the EPSRC Centre for Doctoral Training in the Science and Technology of Fusion Energy.

C.W.W. Haddon and D.P. Hampshire are with Durham University Superconductivity Group, Centre for Material Physics, Department of Physics, Durham University, UK.

Color versions of one or more of the figures in this paper are available online at <https://ieeexplore.ieee.org>.

Digital Object Identifier will be inserted here upon acceptance.

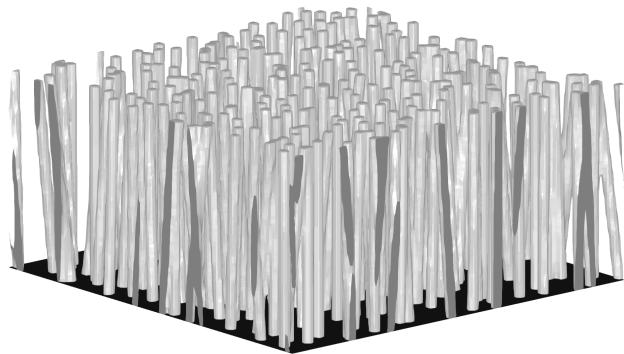


Fig. 1. An isosurface of the condensation parameter in a computational domain representing a REBCO system with splayed nanorods.

Time-dependent Ginzburg–Landau (TDGL) theory can describe the interaction of fluxons with pinning centers, and TDGL simulations have been used successfully to model pinning in coated conductors [10]. But these simulations typically assume that pinning arises due to modulations in the critical temperature only, whilst the other material parameters are constant throughout the matrix and the pins. In order to accurately model insulating oxide nanorods, modulation of the carrier effective mass, which is proportional to the normal state resistivity, must be considered.

For this work, a program was developed to solve the TDGL equations in the high- κ limit [11] whilst allowing all material parameters to vary spatially. Critical current data were produced for pinning landscapes with nanorods of varying density, splay, and normal-state conductivity. A simple geometric multigrid method [12] was adopted to solve the Poisson's equation which constitutes part of the high- κ TDGL system. This significantly improves simulation times and demonstrates the potential for further improvements of a similar magnitude.

II. COMPUTATIONAL METHOD

A. Discretisation of TDGL Equations

Here we consider the limit of large GL parameter, κ , where the field distribution inside a superconductor is uniform and the two TDGL equations are simplified by neglecting the dynamics of the vector potential [11]. We assume a Landau gauge [13] and allow the material parameters to vary in space, taking m^{-1} as a diagonal tensor. Thermal fluctuations are not included.

The TDGL equations are discretized with second-order central-differences in space and the first-order backwards Euler

method in time. In the discrete equations k is the timestep, h is the grid step, I denotes a multi-dimensional index, (I_1, I_2, I_3) , p^I denotes the grid point with index I and coordinates (hI_1, hI_2, hI_3) , and δ_μ denotes an elementary displacement in index space so that $(I + \delta_\mu)_\mu = I_\mu + 1$. For the first TDGL equation, the covariant derivative, $\nabla - i\mathbf{A}$, is discretized using the link variable method [14] and the nonlinear term is linearized by replacing $|\psi|^2$ with the known value at the previous timestep. The discrete equation is given by

$$\begin{aligned} \frac{\psi_1^I - \psi_0^I}{k} + i\varphi^I \psi_1^I &= (\alpha^I - \beta^I |\psi_0^I|^2) \psi_1^I \\ &+ \frac{1}{h^2} \sum_{\mu} \left(m^{-1I} (U_{\mu}^I \psi_1^{I+\delta_{\mu}} - \psi_1^I) \right. \\ &\left. + m^{-1I-\delta_{\mu}} (\bar{U}_{\mu}^{I-\delta_{\mu}} \psi_1^{I-\delta_{\mu}} - \psi_1^I) \right) \end{aligned} \quad (1)$$

where ψ_0^I and ψ_1^I denote the values of the wavefunction at the previous and next timestep respectively, sampled at the point p^I . Likewise, φ^I , α^I , and β^I are evaluated at the grid points, whereas m^{-1I} denotes the average of m^{-1} over the edge connecting p^I and $p^{I+\delta_{\mu}}$ and the link variables are given by

$$U_{\mu}^I = e^{-ihA_{\mu}^I} \approx e^{-i \int_{p^I}^{p^{I+\delta_{\mu}}} A_{\mu}(p) dp_{\mu}} \quad (2)$$

where

$$\mathbf{A}(y) = (yB_{z,\text{ext}} - K)\mathbf{e}_x, \quad (3)$$

$$\begin{aligned} \langle m_x^{-1I} \rangle \frac{K_1 - K_0}{k} &= J_{x,\text{ext}} \\ &- \left\langle \frac{1}{2h} \Im \left\{ \bar{\psi}^I (U_{x,0}^I \psi^{I+\delta_x} - \bar{U}_{x,0}^{I-\delta_x} \psi^{I-\delta_x}) \right\} \right\rangle. \end{aligned} \quad (4)$$

and $E_x = (K_1 - K_0)/k$. The second TDGL equation is discretized using the usual central differences method, giving

$$\begin{aligned} \frac{1}{h^2} \sum_{\mu} \left(m^{-1I} (\varphi^{I+\delta_{\mu}} - \varphi^I) + m^{-1I-\delta_{\mu}} (\varphi^{I-\delta_{\mu}} - \varphi^I) \right) \\ = \frac{1}{h^2} \Im \left\{ \bar{\psi}^I \sum_{\mu} \left(m^{-1I} U_{\mu}^I \psi^{I+\delta_{\mu}} + m^{-1I-\delta_{\mu}} \bar{U}_{\mu}^I \psi^{I-\delta_{\mu}} \right) \right\} \end{aligned} \quad (5)$$

In order to obtain representative critical current densities the domain must be periodic, since surface pinning would otherwise dominate. Periodicity in the direction of the current flow, the x -direction, ensures current continuity and quasiperiodic boundary conditions [13] in the y -direction, prevent surface pinning whilst preserving all gauge-invariant observables, such as the free energy density.

B. Multigrid Method for TDGL

The elliptic Poisson's equation (5) limits the performance of Gauss-Seidel relaxation but is the canonical problem for multigrid methods [12]. The basic idea is to first solve the problem on a coarse grid to resolve low-frequencies, then transfer the solution to the fine grid to resolve the high-frequency components. This is beneficial because the Gauss-Seidel method has superior convergence for error components of high-frequency relative to the grid spacing.

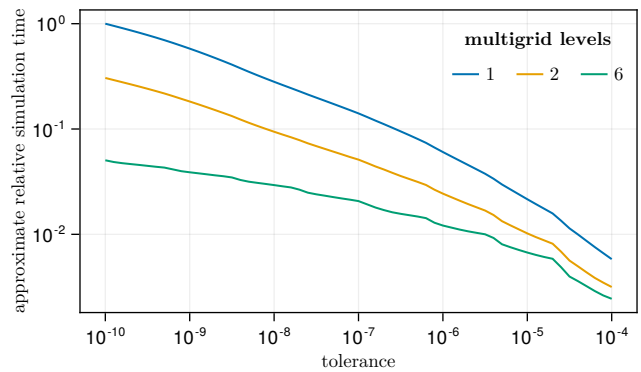


Fig. 2. Comparison of critical-current-simulation times vs. tolerance for varying number of multigrid levels.

A time step consists of solving Equation 1, then taking a forward Euler step with Equation 4, and then solving Equation 5. Equation 1 is solved using a red-black Gauss-Seidel method, with a residual L^∞ norm convergence check and Equation 5 is solved using a geometric multigrid method with a red-black Gauss-Seidel smoother.

Here we consider Equation 5 in the form $L\varphi = f(\psi)$ where L is the linear discrete-Laplacian operator. Given some initial guess φ_e , the residual, r , and the error, ε , are related by

$$L(\varphi_e + \varepsilon) = f(\psi) \implies L\varepsilon = r. \quad (6)$$

Now consider a two-dimensional 2-grid algorithm where the coarse grid has every other row and column removed. One multigrid step consists of calculating the $f(\psi)$ on the fine grid, iterating with an initial guess φ_e , calculating the residual, “restricting” the residual to the coarse grid, iterating Equation 6 using an initial guess $\varepsilon = 0$, interpolating ε to the fine grid, and then correcting φ_e on the fine grid. The full n -grid V-cycle algorithm performs a multigrid iteration instead of Gauss-Seidel on the coarse grid using an even coarser grid, and likewise until the coarsest grid is reached.

Figure 2 demonstrates the advantages of the multigrid method. It shows the approximate running time of a critical current simulation measured relative to a single-grid approach for a range of tolerances. The simulation time was calculated as follows. First, simulations were performed on GPUs with 1, 2, and 6 multigrid levels to a tolerance of 10^{-10} , recording the residual after each multigrid/Gauss-Seidel iteration. Next, the simulations were run on a single core, recording the time for taken for each iteration. It was found that a batch of wavefunction Gauss-Seidel iterations took, on average, 0.88 s, a 1-grid scalar potential iteration took 0.48 s, a 2-grid iteration took 0.67 s, and a 6-grid iteration took 0.74 s. The total simulation time was then calculated by summing the iteration times for those iterations which had residuals greater than the given tolerance. Although the benefits of the multi-grid method are limited for large tolerance calculations, for small tolerances the simulation time can be orders of magnitude faster when using the multigrid method, despite the anisotropy of the matrix and the jump in the effective mass at the pin

boundary, which are known to reduce the advantage of the multigrid method as compared with single-grid methods [15].

C. Material model

The distribution of material parameters in the computational domain is designed to model an anisotropic superconductor with embedded non-superconducting nanorods. Intrinsic defects are not included. The free parameters in TDGL are α , β , and m_i called the condensation parameter, the nonlinearity parameter, and the effective mass. For the superconducting matrix, the z -axis of the system coincides with the crystalline c -axis and is taken to have an anisotropy factor of $\gamma = \xi_{ab}/\xi_c = 3$, which is representative of commercial REBCO tapes [16]. The nanorods are considered circular and isotropic, with a relative condensation parameter of $\alpha = -1$ and an effective mass 10 times that in the a - b plane unless otherwise stated. When the maximum splay angle is $\theta \neq 0$, each nanorod is sheared in a random direction in the x - y plane, by a random amount uniformly distributed in $[0, \arctan \theta]$, about its base at $z = 0$. When the maximum splay angle is zero, each nanorod is a cylinder of radius $r = \xi_{ab}$ aligned with the c -axis. The nanorods are distributed by dividing the x - y plane into rectangles and placing a nanorod at a randomly chosen point in each rectangle. A non-superconducting layer is included in the x - y plane to mimic insulating boundary conditions in the z -direction so that the nanorods can be splayed by arbitrary angles without introducing artificial breaks at the system boundary. The nonlinearity parameter is set to 1 throughout the entire domain. An example of a computational domain with splayed nanorods is shown in Figure 1. The critical current is determined by a well-established upward current ramp procedure [17] using an electric field criterion of $10^{-5} E_0$.

The grid resolution used in the simulation is $h = \frac{1}{2}\xi_{ab}$ and the system dimensions are $64\xi_{ab} \times 64\xi_{ab} \times 32\xi_{ab}$. Since the grid resolution is fairly coarse, the material parameters are first sampled on a high-resolution grid, 4-times the linear resolution of the final simulation, which is then down-sampled to the final grid resolution. In order to implement the boundary condition correctly, it is important for each neighbouring pair of vertices with different condensation parameters ($\alpha = \pm 1$) to be connected by an edge with a large effective mass ($m = 10$), otherwise the order parameter is artificially suppressed at the edge of the superconducting region. To ensure this, when testing whether each edge is inside a nanorod, a larger radius of $r + \frac{1}{2}h = \frac{5}{4}\xi_{ab}$ is used, since the test is performed at the midpoint of the edge.

III. RESULTS

A. Effect of nanorod density

Figure 3 shows the critical current density vs. applied field for highly resistive ($\alpha = -1$, $m = 10$) nanorods aligned with the c -axis with varying density (For YBCO, $J_0 = J_{0,ab} \approx 1.1 \text{ GA/cm}^2$ [18]).

In low fields and for higher pin densities, each fluxon occupies its own pin, and each pin contains at most one fluxon, resulting in a field-independent critical current density. When

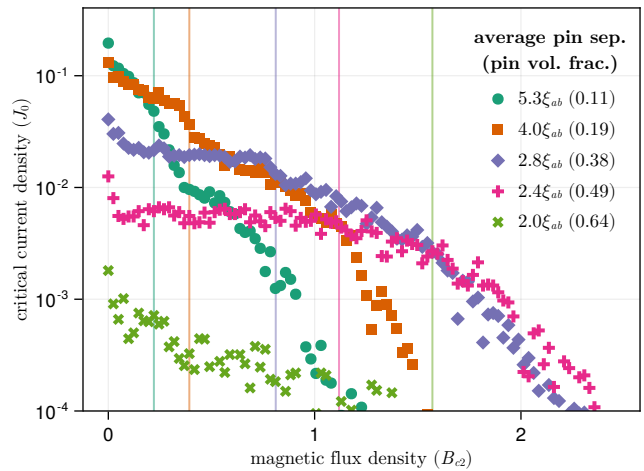


Fig. 3. Critical current density vs. field for aligned highly resistive nanorods with varying density. The separation is the distance between the rod centers. The vertical lines provide matching fields at each pin density.

the number of fluxons approaches the number of pins (i.e. the matching field), fluxons begin to enter the superconducting matrix. Due to the irregular distribution of pins, where some are very close or overlap, this happens just below the matching field. At fields greater than the matching field, the mechanism which limits J_c switches from the de-pinning of single fluxons to the coherent motion of the vortex matter past the pins. For low pin densities this results in a rapid drop in J_c because the vortex matter must shear only slightly to flow past the sparse matrix of pinned fluxons. At high pin densities the fluxons in the matrix are effectively trapped by the pinned fluxons. In this case, the decrease in critical current density is primarily driven by the decrease in the condensate fraction as more fluxons enter the superconducting matrix. Furthermore, there is no significant change in the critical current at B_{c2} , the upper critical field of the matrix, since surface superconductivity persists in the vicinity of the matrix-pin interfaces. In fact, superconductivity can persist to very high fields as the thickness of the superconducting layer between neighboring pins decreases [19]–[21]. For the system with very high pin density, an average pin separation of $2\xi_{ab}$, the pins, whose radii are ξ_{ab} , are sufficiently dense to block the supercurrent flow entirely, resulting in a negligible critical current density for all fields.

Figure 4 shows the fraction of an a - b cross section which has a superfluid density greater than 1% of the equilibrium value vs. field for different pin densities. The dashed vertical lines indicate the “effective upper critical field”, extracted by linearly extrapolating high field pinning force vs. field data derived from the data in Figure 3. Although the effective upper critical field is greater than the upper critical field of the matrix, it does not represent the point at which the superconducting state is destroyed, or even that the critical current density is zero, but rather it is the field at which the pinning force density is small compared to its peak value. The field at which the suppression of the superconducting state is sufficient to block the last percolative current path leads to a

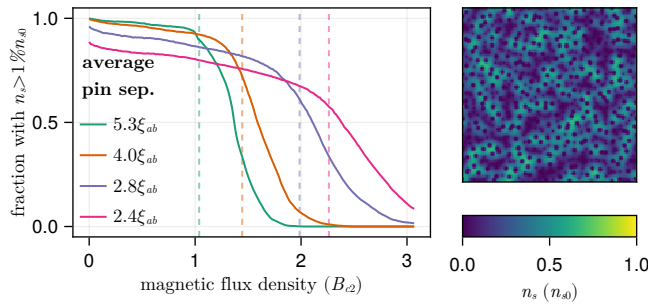


Fig. 4. (Left) Superconducting fraction vs. field for aligned highly resistive nanorods with varying density. Dashed lines indicate the “effective upper critical field” extracted from a linear fit of the high-field tail of the pinning force data derived from Figure 3. (Right) Cross-section in the a - b plane of the superfluid density with an average pin separation of $4.0\xi_{ab}$ at the effective upper critical field of $1.44B_{c2}$.

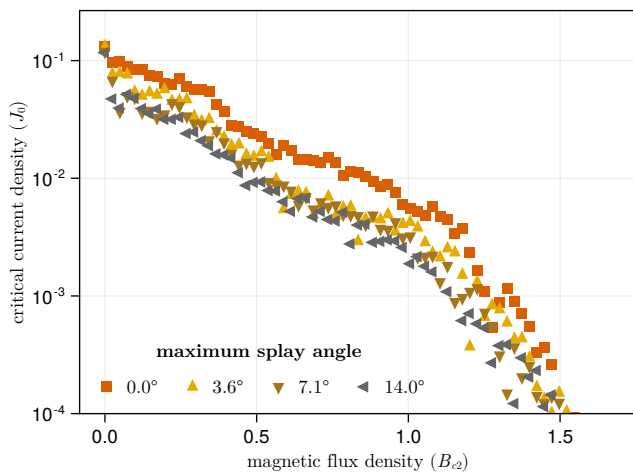


Fig. 5. Critical current density vs. field for highly resistive nanorods with average spacing 4.0ξ and varying maximum splay angle.

precipitous drop in J_c , which is not visible in Figure 3.

B. Effect of nanorod splay

Figure 5 shows the critical current density vs. applied field for highly resistive nanorods with average spacing $4.0\xi_{ab}$ and varying maximum splay angle. Introducing splay reduces the critical current across the whole field range and smooths out the transition from the low-field to the high-field behavior. We attribute this to the reduction in the pinned fluxon length fraction.

In high-current HTS wire with BZO APCs, continuous c -axis-aligned nanorods are associated with increased critical current densities [8], [9], but splayed nanorods have also been associated with increased J_c due to the entanglement of fluxons in the vortex matter ground state [5]–[7]. The fact that a small amount of splay reduces the critical current density, and that J_c is substantially independent of splay for larger angles, indicates that some aspects of the real pinning landscape are not yet captured.

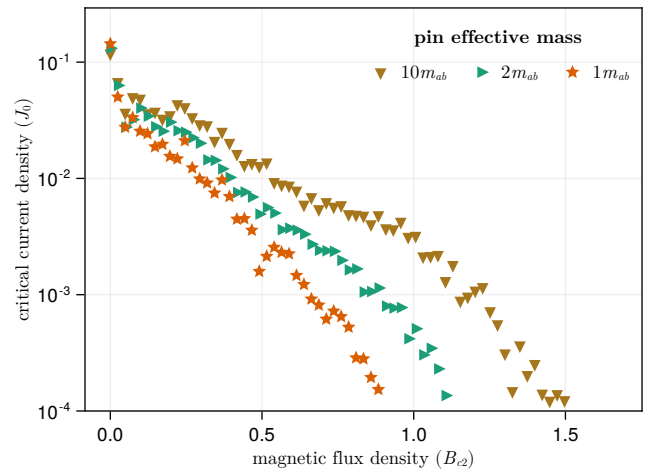


Fig. 6. Critical current density vs. field for nanorods with average spacing 4.0ξ , maximum splay angle 7.1° , and varying effective mass.

C. Effect of nanorod conductivity

Figure 6 shows the critical current density vs. applied field for nanorods with average spacing $4.0\xi_{ab}$, maximum splay angle 7.1° , and varying effective mass, which is proportional to the normal state resistivity. The data for the material with conducting rods ($m = 1m_{ab}$) show the expected precipitous drop in J_c at B_{c2} , whereas the other two materials have non-zero critical currents beyond the upper critical field of the matrix. It is clear that the mechanism which limits J_c in high fields for systems with highly resistive pins is fundamentally different from that of conducting pins. TDGL models which incorporate only variation of the condensation parameter cannot describe this mechanism.

IV. CONCLUSIONS AND FUTURE WORK

A TDGL model of REBCO with highly resistive nanorod APCs has been implemented showing high-field critical current density limited by percolative current flow between regions of internal surface superconductivity in the vicinity of matrix–pin interfaces. Future work will include the strain field which arises due to the lattice parameter mismatch between the matrix and pin material, which is not included in the present model. TDGL simulations were rapidly accelerated by use of a multigrid method to solve the Poisson’s equation for the scalar potential. Future work will apply the multigrid method for the wavefunction equation to enable simulations with finer spatial resolution.

ACKNOWLEDGMENT

This work is funded by EPSRC grant EP/L01663X/1 and the UK Government Department for Business, Energy & Industrial Strategy. Data are available at <https://doi.org/10.15128/r16q182k20z> and associated materials can be found at <https://dro.dur.ac.uk>. Simulations were carried out using the facilities of the NVIDIA CUDA Centre at Durham University. Code is available on request from D.P.H.

REFERENCES

- [1] J. L. MacManus-Driscoll, S. R. Foltyn, Q. X. Jia, H. Wang, A. Serquis, L. Civale, B. Maiorov, M. E. Hawley, M. P. Maley, and D. E. Peterson, "Strongly enhanced current densities in superconducting coated conductors of $\text{YBa}_2\text{Cu}_3\text{O}_{7-x} + \text{BaZrO}_3$," *Nature Materials*, vol. 3, pp. 439–443, 2004.
- [2] Y. Yamada, K. Takahashi, H. Kobayashi, M. Konishi, T. Watanabe, A. Ibi, T. Muroga, S. Miyata, T. Kato, T. Hirayama, and Y. Shiohara, "Epitaxial nanostructure and defects effective for pinning in $\text{Y(RE)Ba}_2\text{Cu}_3\text{O}_{7-x}$ coated conductors," *Applied Physics Letters*, vol. 87, no. 13, p. 132502, 2005.
- [3] A. Goyal, S. Kang, K. J. Leonard, P. M. Martin, A. A. Gapud, M. Varela, M. Paranthaman, A. O. Ijaduola, E. D. Specht, J. R. Thompson, D. K. Christen, S. J. Pennycook, and F. A. List, "Irradiation-free, columnar defects comprised of self-assembled nanodots and nanorods resulting in strongly enhanced flux-pinning in $\text{YBa}_2\text{Cu}_3\text{O}_{7-\delta}$ films," *Superconductor Science and Technology*, vol. 18, no. 11, p. 1533, 2005.
- [4] K. Matsumoto and P. Mele, "Artificial pinning center technology to enhance vortex pinning in YBCO coated conductors," *Superconductor Science and Technology*, vol. 23, no. 1, p. 014001, 2009.
- [5] T. Hwa, P. Le Doussal, D. R. Nelson, and V. M. Vinokur, "Flux pinning and forced vortex entanglement by splayed columnar defects," *Phys. Rev. Lett.*, vol. 71, pp. 3545–3548, Nov 1993.
- [6] L. Civale, L. Krusin-Elbaum, J. R. Thompson, R. Wheeler, A. D. Marwick, M. A. Kirk, Y. R. Sun, F. Holtzberg, and C. Feild, "Reducing vortex motion in $\text{YBa}_2\text{Cu}_3\text{O}_7$ crystals with splay in columnar defects," *Phys. Rev. B*, vol. 50, pp. 4102–4105, Aug 1994.
- [7] F. J. Baca, P. N. Barnes, R. L. S. Emergo, T. J. Haugan, J. N. Reichart, and J. Z. Wu, "Control of BaZrO_3 nanorod alignment in $\text{YBa}_2\text{Cu}_3\text{O}_{7-x}$ thin films by microstructural modulation," *Applied Physics Letters*, vol. 94, no. 10, p. 102512, 2009.
- [8] V. Selvamanickam, M. H. Gharahcheshmeh, A. Xu, E. Galstyan, L. Delgado, and C. Cantoni, "High critical currents in heavily doped $(\text{Gd,Y})\text{Ba}_2\text{Cu}_3\text{O}_x$ superconductor tapes," *Applied Physics Letters*, vol. 106, no. 3, p. 032601, 2015.
- [9] V. Selvamanickam, M. H. Gharahcheshmeh, A. Xu, Y. Zhang, and E. Galstyan, "Critical current density above 15 MA cm^{-2} at 30 K, 3 T in $2.2 \mu\text{m}$ thick heavily-doped $(\text{Gd,Y})\text{Ba}_2\text{Cu}_3\text{O}_x$ superconductor tapes," *Superconductor Science and Technology*, vol. 28, no. 7, p. 072002, 2015.
- [10] I. A. Sadovskyy, A. E. Koshelev, A. Glatz, V. Ortalan, M. W. Rupich, and M. Leroux, "Simulation of the vortex dynamics in a real pinning landscape of $\text{YBa}_2\text{Cu}_3\text{O}_{7-\delta}$ coated conductors," *Physical Review Applied*, vol. 5, p. 014011, 2016.
- [11] H. G. Kaper and H. Nordborg, "The frozen-field approximation and the Ginzburg–Landau equations of superconductivity," *Journal of Engineering Mathematics*, vol. 39, pp. 221–240, 2001.
- [12] A. Brandt, "Multi-level adaptive solutions to boundary-value problems," *Mathematics of Computation*, vol. 31, no. 138, pp. 333–390, 1977.
- [13] I. A. Sadovskyy, A. E. Koshelev, C. L. Phillips, D. A. Karpeyev, and A. Glatz, "Stable large-scale solver for Ginzburg–Landau equations for superconductors," *Journal of Computational Physics*, vol. 294, pp. 639–654, 2015.
- [14] W. D. Gropp, H. G. Kaper, G. K. Leaf, D. M. Levine, M. Palumbo, and V. M. Vinokur, "Numerical simulation of vortex dynamics in type-II superconductors," *Journal of Computational Physics*, vol. 123, no. 2, pp. 254–266, 1996.
- [15] W. L. Briggs, V. E. Henson, and S. F. McCormick, *A Multigrid Tutorial*, 2nd ed. Philadelphia: SIAM, 2000.
- [16] A. P. Smith, M. J. Raine, E. Surrey, S. Awaji, T. Okada, and D. P. Hampshire, "3-D properties in (RE)BCO tapes measured in fields up to 35 T," *IEEE Transactions on Applied Superconductivity*, vol. 29, no. 5, pp. 1–5, 2019.
- [17] A. I. Blair and D. P. Hampshire, "Modeling the critical current of polycrystalline superconducting films in high magnetic fields," *IEEE Transactions on Applied Superconductivity*, vol. 29, no. 5, pp. 1–5, 2019.
- [18] G. Wang, M. J. Raine, and D. P. Hampshire, "How resistive must grain boundaries in polycrystalline superconductors be, to limit J_c ?" *Superconductor Science and Technology*, vol. 30, no. 10, p. 104001, Aug 2017.
- [19] V. L. Ginzburg and L. D. Landau, "On the theory of superconductivity," *Journal of Experimental and Theoretical Physics*, vol. 20, pp. 1064–1082, 1950.
- [20] A. I. Buzdin, "Multiple-quanta vortices at columnar defects," *Phys. Rev. B*, vol. 47, pp. 11 416–11 419, May 1993.
- [21] A. Bezryadin and B. Pannetier, "Edge superconducting states," *Physica Scripta*, vol. 1996, no. T66, p. 225, Jan 1996.